

# Provably unconditionally stable, second-order time-accurate, mixed variational methods for phase-field models

Hector Gomez <sup>a,\*</sup>, Thomas J.R. Hughes <sup>b</sup>

<sup>a</sup> Group of Numerical Methods in Engineering, University of A Coruña, Department of Mathematical Methods, Campus de Elviña, s/n 15192 A Coruña, Spain

<sup>b</sup> Institute for Computational Engineering and Sciences, The University of Texas at Austin, 1 University Station C0200, 201 E. 24th Street, Austin, TX 78712, United States

## ARTICLE INFO

### Article history:

Received 26 September 2010

Received in revised form 10 January 2011

Accepted 18 March 2011

Available online 31 March 2011

### Keywords:

Nonlinear stability

Phase-field

Mixed finite element

Time integration

Cahn–Hilliard

## ABSTRACT

We introduce provably unconditionally stable mixed variational methods for phase-field models. Our formulation is based on a mixed finite element method for space discretization and a new second-order accurate time integration algorithm. The fully-discrete formulation inherits the main characteristics of conserved phase dynamics, namely, mass conservation and nonlinear stability with respect to the free energy. We illustrate the theory with the Cahn–Hilliard equation, but our method may be applied to other phase-field models. We also propose an adaptive time-stepping version of the new time integration method. We present some numerical examples that show the accuracy, stability and robustness of the new method.

© 2011 Elsevier Inc. All rights reserved.

## 1. Introduction

The phase-field method is a recently introduced mathematical theory for modeling interfacial phenomena (see [2] for a brief introduction in the context of fluid mechanics). The key idea of the phase-field methodology is to replace sharp interfaces by thin transition regions where interfacial forces are smoothly distributed. These transition layers (also called diffuse interfaces) are part of the solution of the phase-field equations and, thus, front-tracking is not necessary. Another fundamental feature of phase-field models is that diffuse interfaces are described by higher-order partial-differential operators.

The phase-field method was originally devised for microstructure evolution [14,27] and phase transition [36,52,62,76], but it has been recently used to model foams [31], planet formation [71], ferroelectric ceramics [42,54], dendritic growth [48,51], phase separation of block copolymers [15], growth of cancerous tumors [20,32,61], solid–solid transitions [33,57,58], infiltration of water into a porous medium [21,22], dewetting and rupture of thin liquid films [9] and many other phenomena.

One of the main reasons for the success of the phase-field methodology is that it is based on rigorous mathematics and thermodynamics. Most phase-field models satisfy a nonlinear stability relationship, usually expressed as a time-decreasing free-energy functional. The goal of this paper is to devise space and time discretization schemes that inherit the nonlinear stability relationship of the continuous model.

The idea of designing numerical techniques that satisfy thermodynamic relations at the discrete level has been extensively studied in the context of solid [3,60,66,67] and fluid mechanics [39,45,69,70], but it is significantly less developed in the realm of phase-field models. The first study we know of was carried out by Du and Nicolaides [24] who derived a

\* Corresponding author.

E-mail address: [hgomez@udc.es](mailto:hgomez@udc.es) (H. Gomez).

second-order accurate unconditionally stable time-stepping scheme for a simplified version of the Cahn–Hilliard equation. This paper was followed up by several works of an analytical character, but to our knowledge, it has not been applied to large scale calculations. In fact, we applied this method to the general version of the Cahn–Hilliard equation and obtained poor numerical results. Later on, Eyre [28] derived a first-order accurate unconditionally stable time-stepping scheme for a simplified version of the Cahn–Hilliard equation. Although Eyre’s work is unpublished, it has had significant impact. Eyre’s method has been extensively used by the computational community and it has served as inspiration for many other time integration schemes. Other significant works, which deal with simplified versions of the Cahn–Hilliard equation, are due to de Mello et al. [59], Furihata [34], He and Liu [40], Kim et al. [50] and Vollmayr-Lee and Rutemberg [73]. Other noteworthy contributions for the phase-field crystal equation and a bistable epitaxial thin film equation are due to Hu et al. [41] and Xu and Tang [75], respectively.

In this paper we introduce provably unconditionally stable, second-order time accurate schemes for phase-field models. We illustrate the theory using the Cahn–Hilliard equation, but the method may also be applied to other phase-field models. We present the method for a spatial discretization based on a mixed finite element formulation, but we feel that our time integration scheme may also be applied to finite difference or spectral collocation spatial discretizations, which are ubiquitous in computational phase-field modeling.

The rest of the paper is organized as follows: in Section 2 we briefly review the derivation of the Cahn–Hilliard equation to illustrate its conservation and stability properties, which will be inherited by our numerical scheme. Section 3 presents our space and time discretizations. In Section 4 we present some numerical examples that illustrate the accuracy, stability and robustness of the proposed method. We draw conclusions in Section 5.

## 2. The Cahn–Hilliard equation

The Cahn–Hilliard equation describes the separation of mixtures with a miscibility gap in their phase diagrams and it is probably the most widely known phase-field model. The Cahn–Hilliard equation is derived from the Ginzburg–Landau free energy [53], which we describe in the following section.

### 2.1. The Ginzburg–Landau free energy

We focus on isothermal binary mixtures. In this setting, the thermodynamic state of the mixture is defined by a single scalar field  $c$  representing the concentration of one of the species. The concentration of the other component is  $1 - c$ . Assuming that the mixture is contained within an open domain  $\Omega \subset \mathbb{R}^3$ , the Ginzburg–Landau free energy is defined by the functional,

$$\mathcal{E}(c) = \int_{\Omega} (\Psi_c + \Psi_s) d\mathbf{x} \quad (1)$$

where  $\Psi_c$  is the chemical free energy and  $\Psi_s$  is the surface free energy. According to the original model of Cahn and Hilliard [12,13], the chemical free energy is given by

$$\Psi_c = NkT(c \log c + (1 - c) \log(1 - c)) + N\omega c(1 - c) \quad (2)$$

while the surface free energy takes on the form

$$\Psi_s = \frac{1}{2} \lambda |\nabla c|^2 \quad (3)$$

In Eqs. (2) and (3),  $N$  is the number of molecules per unit volume,  $k$  is the Boltzmann’s constant,  $T$  is the absolute temperature and  $\omega$  is an interaction energy defined by

$$\omega = 2kT_c \quad (4)$$

In Eq. (4)  $T_c$  is the so-called critical temperature, that is, the maximum temperature at which phase separation is possible. Finally,  $\lambda$  is a positive constant defined as

$$\lambda = N\omega\epsilon^2 \quad (5)$$

where  $\epsilon$  is a length scale of the problem.

For  $\theta_m = T_c/T \leq 1$  the chemical free energy has a single well and admits only one phase. In contrast, for  $\theta_m > 1$ , it is non-convex, with two local minima to which the concentration is driven. These local minima are called binodal points. The binodal points are not the pure phases, although they are close to them for physically relevant values of the parameters. In this paper we will focus on the case  $\theta_m > 1$ .

## 2.2. The Cahn–Hilliard equation

Our numerical scheme inherits the conservation and dissipation properties of the Cahn–Hilliard equation. As a consequence, we feel that it is important to start off with the classical derivation of the Cahn–Hilliard equation, which clearly illustrates those properties. The starting point is the mass balance law,

$$\frac{\partial c}{\partial t} + \nabla \cdot \mathbf{J} = 0 \quad (6)$$

where  $\mathbf{J}$  is the mass flux defined as

$$\mathbf{J} = -M(c) \nabla \left( \frac{\delta \mathcal{E}}{\delta c} \right) \quad (7)$$

In Eq. (7)  $M$  is a nonlinear and positive function, the mobility, and

$$\frac{\delta \mathcal{E}}{\delta c} = \mu(c) - \lambda \Delta c \quad (8)$$

denotes the variational derivative of the functional  $\mathcal{E}$ . Finally,  $\mu$  is the chemical potential, that is, the derivative of the chemical free energy with respect to  $c$ . Gathering Eqs. (6)–(8) we get the Cahn–Hilliard equation

$$\frac{\partial c}{\partial t} = \nabla \cdot (M(c) \nabla (\mu(c) - \lambda \Delta c)) \quad (9)$$

This is the standard derivation of the Cahn–Hilliard phase-field model. For an alternative derivation based on a microforce balance, the reader is referred to [37]. The previous derivation clearly shows (see Eq. (6)) that the Cahn–Hilliard equation conserves the mass of the mixture as time evolves. It can also be proven that the Ginzburg–Landau free energy does not increase with time. The latter result can be obtained multiplying (9) with the variational derivative of the free energy. If we define the real-valued function  $E(t) = \mathcal{E}(c(\cdot, t))$ , it follows that

$$\frac{dE}{dt} = - \int_{\Omega} \nabla (\mu(c) - \lambda \Delta c) M(c) \nabla (\mu(c) - \lambda \Delta c) d\mathbf{x} \leq 0 \quad (10)$$

We consider (10) the fundamental stability property of the Cahn–Hilliard equation.

### Remarks

- (1) In most analytic studies and numerical simulations the mobility is assumed to be a positive constant. This assumption significantly simplifies the mathematical analysis and the numerical simulation of the Cahn–Hilliard equation. However, to accurately describe the physics of phase separation, pure phases must have vanishing mobility. A positive function of  $c$  satisfying this requirement is called degenerate mobility. The most common choice in the literature is

$$M(c) = Dc(1 - c) \quad (11)$$

where  $D$  is a positive constant. We will use the mobility defined in (11) throughout this paper.

- (2) Due to the complexity of the function  $\Psi_c$ , some simpler approximations are normally employed. In particular, a polynomial of degree four has been used to approximate the chemical free energy in most analytic studies and numerical simulations. The quartic polynomial may be an acceptable approximation of the chemical free energy for shallow quenches, but it is a poor approximation for deep quenches [17]. Moreover, the solution to the Cahn–Hilliard equation with the quartic polynomial and constant mobility may take values outside the physical range  $c \in [0, 1]$  (see the work of Elliot and Garcke [26]). This demonstrates the importance of developing numerical algorithms that can handle the logarithmic free energy. In what follows we will focus on the logarithmic chemical free energy defined in (2). For further reference, we note that  $\mu''' = \Psi_c^{iv} > 0$ , which may be easily verified. This property is important in the sequel.
- (3) In order to define a well posed initial/boundary-value problem, Eq. (9) needs to be complemented with suitable initial and boundary conditions. Let us assume that Eq. (9) is posed on a space/time domain  $\Omega \times (0, T)$ , where  $\Omega$  is an open subset of  $\mathbb{R}^3$  and  $(0, T)$  is the time interval. We assume that  $\Omega$  has a smooth boundary  $\Gamma$  with unit outward normal  $\mathbf{n}$ . A suitable initial condition consists of setting the concentration field at the initial time. Regarding boundary conditions, there are several options. Probably the most common choice in the literature is to assume periodic boundary conditions (the reason for this may be that the literature on numerical methods for the Cahn–Hilliard equation is dominated by spectral methods). Another option, considered a better alternative by some authors [59], is setting on the boundary

$$\nabla c \cdot \mathbf{n} = 0 \quad (12)$$

$$M(c) \nabla (\mu(c) - \lambda \Delta c) = 0 \quad (13)$$

Eqs. (12) and (13) may be considered as natural boundary conditions for the Cahn–Hilliard equation in a variational formulation.

### 3. Numerical formulation

#### 3.1. Continuous problem in the weak form

Our theory is based on a mixed finite element [43] formulation of the Cahn–Hilliard equation. Thus, we split Eq. (9) as

$$\frac{\partial c}{\partial t} = \nabla \cdot (M(c) \nabla v) \quad \text{in } \Omega \times (0, T) \quad (14)$$

$$v = \mu(c) - \lambda \Delta c \quad \text{in } \Omega \times (0, T) \quad (15)$$

Let  $\mathcal{V}$  denote the trial solution and the weighting functions spaces which are assumed to be the same. Eqs. (14) and (15) can be recast in the weak form as: find  $c, v \in \mathcal{V}$  such that for all  $w, q \in \mathcal{V}$

$$\left( w, \frac{\partial c}{\partial t} \right)_{\Omega} + (\nabla w, M(c) \nabla v)_{\Omega} = 0 \quad (16)$$

$$(q, v)_{\Omega} - (q, \mu(c))_{\Omega} - (\nabla q, \lambda \nabla c)_{\Omega} = 0 \quad (17)$$

where  $(\cdot, \cdot)_{\Omega}$  denotes the  $\mathcal{L}^2$  inner product over the domain  $\Omega$ .

The integration by parts of the previous equations under the assumption of sufficient regularity leads to the Euler–Lagrange form of (16) and (17),

$$\left( w, \frac{\partial c}{\partial t} - \nabla \cdot (M(c) \nabla v) \right)_{\Omega} + (w, M(c) \nabla v \cdot \mathbf{n})_{\Gamma} = 0 \quad (18)$$

$$(q, v - \mu(c) + \lambda \Delta c)_{\Omega} - (q, \lambda \nabla c \cdot \mathbf{n})_{\Gamma} = 0 \quad (19)$$

Eqs. (18) and (19) enforce weak satisfaction of the partial-differential Eq. (9) and boundary conditions (12) and (13).

#### 3.2. Semidiscrete formulation

To perform the space discretization of (16) and (17) we make use of the Galerkin method. We approximate (16) and (17) by the following finite-dimensional problem over the finite element space  $\mathcal{V}^h \subset \mathcal{V}$ . The problem can be stated as: find  $c^h, v^h \in \mathcal{V}^h$  such that for all  $w^h, q^h \in \mathcal{V}^h$

$$\left( w^h, \frac{\partial c^h}{\partial t} \right)_{\Omega} + (\nabla w^h, M(c^h) \nabla v^h)_{\Omega} = 0 \quad (20)$$

$$(q^h, v^h - \mu(c^h))_{\Omega} - (\nabla q^h, \lambda \nabla c^h)_{\Omega} = 0 \quad (21)$$

In the previous equations  $c^h$  takes on the form

$$c^h(\mathbf{x}, t) = \sum_{A=1}^{n_b} c_A(t) N_A(\mathbf{x}) \quad (22)$$

where  $n_b$  is the dimension of the discrete space, the  $N_A$ 's are the basis functions of the discrete space, and the  $c_A$ 's are the coordinates of  $c^h$  on  $\mathcal{V}^h$ . The rest of the variables utilized in (20) and (21) are defined analogously to  $c^h$ .

#### Remark

- (1) We use the same discrete space for  $c^h$  and  $v^h$ . This type of mixed finite element formulation was shown to lead to stable space discretizations in [17,30] (a somewhat different mixed finite element formulation was employed in [74]).
- (2) We will use Non-Uniform Rational B-Splines (NURBS) basis functions to define our discrete spaces. For an introduction to NURBS see [63] or [65]. The use of the NURBS technology in the context of analysis has led to the concept of Isogeometric Analysis, which is a generalization of finite element analysis with several advantages [4,6–8,11,19,25,29,35,44,56]. For a detailed description of Isogeometric Analysis, the reader is referred to [18].

#### 3.3. Time integration

Our time integration scheme is based on the following splitting of the chemical free-energy,

$$\Psi_c = \Psi_1 + \Psi_2 \quad (23)$$

where  $\Psi_1^{iv} \geq 0$ ,  $\Psi_2^{iv} \leq 0$  and  $\Psi_{\square}^{iv}$  denotes the fourth derivative of  $\Psi_{\square}$ . This decomposition always exists, but it is not unique. For the Cahn–Hilliard equation, the splitting is just

$$\Psi_1 = \Psi_c; \quad \Psi_2 = 0 \quad (24)$$

but for other phase-field models  $\Psi_1$  and  $\Psi_2$  will be both nonzero, so we will assume that  $\Psi_1 \neq 0$  and  $\Psi_2 \neq 0$  to present our new method in its full generality.

In the sequel we will make use of the notation  $\mu_1 = \Psi'_1$ ,  $\mu_2 = \Psi'_2$  and, thus

$$\mu_1''' \geq 0, \quad \mu_2''' \leq 0 \quad (25)$$

Our time integration algorithm may be described as follows: Let us assume that the time interval  $\mathcal{I} = (0, T)$  is divided into  $N$  subintervals  $\mathcal{I}_n = (t_n, t_{n+1})$ ,  $n = 0, \dots, N-1$ . We use the notation  $c_n^h$  and  $v_n^h$  for the fully discrete solutions. Our time integration scheme may be defined as follows: Given  $c_n^h$  and  $v_n^h$ , find  $c_{n+1}^h$ ,  $v_{n+1}^h$  such that for all  $w^h$ ,  $q^h \in \mathcal{V}^h$

$$\left( w^h, \frac{[c_n^h]}{\Delta t_n} \right)_\Omega + (\nabla w^h, M(c_{n+\alpha}^h) \nabla v_{n+1}^h)_\Omega = 0 \quad (26)$$

$$\begin{aligned} (q^h, v_{n+1}^h)_\Omega - \left( q^h, \frac{1}{2} (\mu(c_n^h) + \mu(c_{n+1}^h)) - \frac{[c_n^h]^2}{12} (\mu_1''(c_n^h) + \mu_2''(c_{n+1}^h)) \right)_\Omega \\ - (\nabla q^h, \lambda \nabla c_{n+\alpha}^h)_\Omega = 0 \end{aligned} \quad (27)$$

where

$$\Delta t_n = t_{n+1} - t_n, \quad (28)$$

$$[c_n^h] = c_{n+1}^h - c_n^h, \quad (29)$$

$$c_{n+\alpha}^h = c_n^h + \alpha [c_n^h] \quad (30)$$

In Eq. (30),  $\alpha$  is a real-valued parameter that controls the accuracy and stability of the method. We define  $\alpha$  as

$$\alpha = 1/2 + \eta \quad (31)$$

In Eq. (31),  $\eta$  takes on the form

$$\eta = \frac{1}{2} \tanh \left( \frac{\Delta t_n}{\delta} \right) \quad (32)$$

where  $\delta$  is an intrinsic time scale of the problem. We define  $\delta$  making use of a natural time scale of the Cahn–Hilliard equation, namely,  $\lambda/D$ . Thus, we assume that

$$\delta = C \frac{\lambda}{D} \quad (33)$$

where  $C$  is a nondimensional constant that takes the value  $C = 10^3$ . We will use this value of  $C$  for *all* the numerical examples in this paper. However, we remark that this parameter may be used to increase the robustness or the accuracy of the method when necessary. In general, larger values of  $C$  render a more accurate method and smaller values of  $C$  lead to a more robust algorithm. This can be understood mathematically by examining Eq. (42).

The following theorem summarizes the main features of our numerical scheme.

**Theorem 1.** *The fully-discrete variational formulation (26)–(32):*

(1) *Verifies mass conservation, that is,*

$$\int_\Omega c_n^h d\mathbf{x} = \int_\Omega c_0^h d\mathbf{x} \quad \forall n = 1, \dots, N$$

(2) *Verifies the nonlinear stability condition*

$$\mathcal{E}(c_n^h) \leq \mathcal{E}(c_{n-1}^h) \quad \forall n = 1, \dots, N$$

(3) *Gives rise to a local truncation error  $\tau$  that may be bounded as  $|\tau(t_n)| \leq K \Delta t_n^2$  for all  $t_n \in [0, T]$ , where  $K$  is a constant independent of  $\Delta t_n$ .*

**Proof**

(1) Taking  $w^h = 1$  in Eq. (26), it follows by induction that

$$\int_\Omega c_n^h d\mathbf{x} = \int_\Omega c_0^h d\mathbf{x} \quad \forall n = 1, \dots, N$$

(2) Let  $f : [a, b] \mapsto \mathbb{R}$  be a sufficiently smooth function. We will make use of the following quadrature formulas:

$$\int_a^b f(x) dx = \frac{b-a}{2} (f(a) + f(b)) - \frac{(b-a)^3}{12} f''(a) - \frac{(b-a)^4}{24} f'''(\xi); \quad \xi \in (a, b) \quad (34)$$

$$\int_a^b f(x) dx = \frac{b-a}{2} (f(a) + f(b)) - \frac{(b-a)^3}{12} f''(b) + \frac{(b-a)^4}{24} f'''(\zeta); \quad \zeta \in (a, b) \quad (35)$$

Since these quadrature formulas are new as far as we are aware, we provide a complete derivation of one of them in the Appendix (the derivation of the other is analogous). Let us apply the quadrature formula (34) to the right-hand side of the identity

$$\int_{c_n^h}^{c_{n+1}^h} \Psi'_k(t) dt = \int_{c_n^h}^{c_{n+1}^h} \mu_k(t) dt; \quad k = 1, 2 \quad (36)$$

with  $k = 1$ . Basic algebraic manipulation leads to the expression

$$\frac{\llbracket \Psi_1(c_n^h) \rrbracket}{\llbracket c_n^h \rrbracket} + \frac{\llbracket c_n^h \rrbracket^3}{24} \mu_1'''(c_{n+\xi}^h) = \frac{1}{2} (\mu_1(c_n^h) + \mu_1(c_{n+1}^h)) - \frac{\llbracket c_n^h \rrbracket^2}{12} \mu_1''(c_n^h); \quad \xi \in (0, 1) \quad (37)$$

Applying the quadrature formula (35) to the right-hand side of (36) with  $k = 2$ , it follows that

$$\frac{\llbracket \Psi_2(c_n^h) \rrbracket}{\llbracket c_n^h \rrbracket} - \frac{\llbracket c_n^h \rrbracket^3}{24} \mu_2'''(c_{n+\zeta}^h) = \frac{1}{2} (\mu_2(c_n^h) + \mu_2(c_{n+1}^h)) - \frac{\llbracket c_n^h \rrbracket^2}{12} \mu_2''(c_{n+1}^h); \quad \zeta \in (0, 1) \quad (38)$$

Taking  $w^h = v_{n+1}^h$  in (26) and  $q^h = \llbracket c_n^h \rrbracket / \Delta t_n$  in (27) and applying Eqs. (37) and (38), we get

$$-(\nabla v_{n+1}^h, M(c_{n+\alpha}^h) \nabla v_{n+1}^h)_\Omega - \left( \frac{\llbracket c_n^h \rrbracket}{\Delta t_n}, \frac{\llbracket \Psi_c(c_n^h) \rrbracket}{\llbracket c_n^h \rrbracket} + \frac{\llbracket c_n^h \rrbracket^3}{24} (\mu_1'''(c_{n+\xi}^h) - \mu_2'''(c_{n+\zeta}^h)) \right)_\Omega - \left( \nabla \left( \frac{\llbracket c_n^h \rrbracket}{\Delta t_n} \right), \lambda \nabla c_{n+\alpha}^h \right)_\Omega = 0 \quad (39)$$

Using the relation  $c_{n+\alpha}^h = c_{n+1/2}^h + \eta \llbracket c_n^h \rrbracket$ , it follows that:

$$\begin{aligned} & -(\nabla v_{n+1}^h, M(c_{n+\alpha}^h) \nabla v_{n+1}^h)_\Omega - \frac{1}{\Delta t_n} \int_\Omega \llbracket \Psi_c(c_n^h) \rrbracket d\Omega - \left( \frac{\llbracket c_n^h \rrbracket^4}{24 \Delta t_n}, \mu_1'''(c_{n+\xi}^h) - \mu_2'''(c_{n+\zeta}^h) \right)_\Omega \\ & - \left( \nabla \left( \frac{\llbracket c_n^h \rrbracket}{\Delta t_n} \right), \lambda \nabla c_{n+1/2}^h \right)_\Omega - \left( \nabla \llbracket c_n^h \rrbracket, \lambda \frac{\eta}{\Delta t_n} \nabla \llbracket c_n^h \rrbracket \right)_\Omega = 0. \end{aligned} \quad (40)$$

Making use of the identity

$$\left( \nabla \llbracket c_n^h \rrbracket, \lambda \nabla c_{n+1/2}^h \right)_\Omega = \int_\Omega \frac{\lambda}{2} \llbracket |\nabla c^h|^2 \rrbracket d\mathbf{x} \quad (41)$$

we conclude that

$$\frac{\llbracket \mathcal{E}(c^h) \rrbracket}{\Delta t_n} = -(\nabla v_{n+1}^h, M(c_{n+\alpha}^h) \nabla v_{n+1}^h)_\Omega - \left( \frac{\llbracket c_n^h \rrbracket^4}{24 \Delta t_n}, \mu_1'''(c_{n+\xi}^h) - \mu_2'''(c_{n+\zeta}^h) \right)_\Omega - \left( \nabla \llbracket c_n^h \rrbracket, \lambda \frac{\eta}{\Delta t_n} \nabla \llbracket c_n^h \rrbracket \right)_\Omega \quad (42)$$

Since  $\mu_1'''(c) \geq 0$  and  $\mu_2'''(c) \leq 0$ , it follows that:

$$\llbracket \mathcal{E}(c^h) \rrbracket \leq 0 \quad (43)$$

which completes the proof.

(3) We derive a bound on the local truncation error by comparing our method with a known second-order accurate method, the midpoint rule, given as follows:

$$\left( w^h, \frac{\llbracket c_n^h \rrbracket}{\Delta t_n} \right)_\Omega + (\nabla w^h, M(c_{n+1/2}^h) \nabla v_{mid}^h)_\Omega = 0 \quad (44)$$

$$(q^h, v_{mid}^h)_\Omega = (q^h, \mu(c_{n+1/2}^h))_\Omega + (\nabla q^h, \lambda \nabla c_{n+1/2}^h)_\Omega \quad (45)$$

The expression for the local truncation error is obtained by replacing the time discrete solution  $c_n^h$  with the time continuous solution  $c^h(t_n)$  in the above equations. The time continuous solution does not satisfy Eqs. (44) and (45), giving rise to the local truncation error,

$$\left( w^h, \frac{\llbracket c^h(t_n) \rrbracket}{\Delta t_n} \right)_\Omega + (\nabla w^h, M(c^h(t_{n+1/2})) \nabla \tilde{v}_{mid}^h)_\Omega = (w^h, \tau_{mid})_\Omega \quad (46)$$

$$(q^h, \tilde{v}_{mid}^h)_\Omega = (q^h, \mu(c^h(t_{n+1/2})))_\Omega + (\nabla q^h, \lambda \nabla c^h(t_{n+1/2}))_\Omega \quad (47)$$

where  $\tau_{mid}$  is the local truncation error. Assuming sufficient smoothness, Taylor series can be utilized to show that  $\tau_{mid} = \mathcal{O}(\Delta t_n^2)$ . Proceeding in similar fashion with our algorithm, we obtain

$$(w^h, \tau)_\Omega = \left( w^h, \frac{\llbracket c^h(t_n) \rrbracket}{\Delta t_n} \right)_\Omega + (\nabla w^h, M(c^h(t_{n+\alpha})) \nabla \tilde{v}^h)_\Omega \quad (48)$$

$$(q^h, \tilde{v}^h)_\Omega = \left( q^h, \frac{1}{2} (\mu(c^h(t_n)) + \mu(c^h(t_{n+1}))) \right)_\Omega - \left( q^h, \frac{\llbracket c^h(t_n) \rrbracket^2}{12} (\mu_1''(c^h(t_n)) + \mu_2''(c^h(t_{n+1}))) \right)_\Omega \\ + (\nabla q^h, \lambda \nabla c^h(t_{n+\alpha}))_\Omega \quad (49)$$

Assuming smoothness, Taylor series can be utilized to prove

$$\frac{1}{2} (\mu(c^h(t_n)) + \mu(c^h(t_{n+1}))) = \mu(c^h(t_{n+1/2})) + \mathcal{O}(\Delta t_n^2) \quad (50)$$

$$\frac{\llbracket c^h(t_n) \rrbracket^2}{12} (\mu_1''(c^h(t_n)) + \mu_2''(c^h(t_{n+1}))) = \mathcal{O}(\Delta t_n^2) \quad (51)$$

Let us use the identity

$$c^h(t_{n+\alpha}) = c^h(t_{n+1/2}) + \mathcal{O}(\eta \Delta t_n) \quad (52)$$

Considering that

$$\eta = \frac{1}{2} \tanh\left(\frac{\Delta t_n}{\delta}\right) \leq \frac{\Delta t_n}{2\delta} \quad (53)$$

we conclude that

$$c^h(t_{n+\alpha}) = c^h(t_{n+1/2}) + \mathcal{O}(\Delta t_n^2) \quad (54)$$

Combining all these results, it follows that

$$(q^h, \tilde{v}^h)_\Omega = (q^h, \tilde{v}_{mid}^h)_\Omega + \mathcal{O}(\Delta t_n^2) \quad (55)$$

$$(w^h, \tau)_\Omega = (w^h, \tau_{mid})_\Omega + \mathcal{O}(\Delta t_n^2) \quad (56)$$

which completes the proof.  $\square$

## Remarks

- (1) Our new algorithm may be viewed as a second-order perturbation of the midpoint rule which achieves unconditional stability, in contrast with the midpoint rule.
- (2) It is worth further analyzing the stability relationship (42). The first term on the right hand side is what we may call physical dissipation. That term mimics the right hand side of Eq. (10). The last two terms of Eq. (42) may be considered numerical dissipation. Note that these terms vanish as the time step tends to zero. When the time step is large, those terms enhance the stability properties of the scheme, rendering a very robust method.

## 3.4. Numerical implementation

Let  $C_n$  and  $V_n$  be the vector of global degrees of freedom of  $c_n^h$  and  $v_n^h$ , respectively. Our time stepping scheme may be implemented as follows: given  $C_n$  and  $V_n$ , find  $C_{n+1}$ ,  $V_{n+1}$ , such that,

$$\mathbf{R}^M(C_{n+1}, V_{n+1}) = 0 \quad (57)$$

$$\mathbf{R}^E(C_{n+1}, V_{n+1}) = 0 \quad (58)$$

where the above residual vectors are defined as

$$\mathbf{R}^M = \{R_A^M\} \quad (59)$$

$$R_A^M = \left( N_A, \frac{\llbracket C_n^h \rrbracket}{\Delta t_n} \right)_\Omega + (\nabla N_A, M(c_{n+\alpha}^h) \nabla v_{n+1}^h)_\Omega \quad (60)$$

$$\mathbf{R}^E = \{R_A^E\} \quad (61)$$

$$R_A^E = -(N_A, v_{n+1}^h)_\Omega + \left( N_A, \frac{1}{2} (\mu(c_n^h) + \mu(c_{n+1}^h)) - \frac{\llbracket C_n^h \rrbracket^2}{12} (\mu_1''(c_n^h) + \mu_2''(c_{n+1}^h)) \right)_\Omega + (\nabla N_A, \lambda \nabla c_{n+\alpha}^h)_\Omega \quad (62)$$

Eqs. (57) and (58) constitute a nonlinear system of algebraic equations that needs to be solved at each time step. We linearize system (57) and (58) using Newton's method which leads to a two-stage predictor multicorrector algorithm, that may be described as follows,

*Predictor stage:* Set

$$\mathbf{C}_{n+1,(0)} = \mathbf{C}_n \quad (63)$$

$$\mathbf{V}_{n+1,(0)} = \mathbf{V}_n \quad (64)$$

where the subscript 0 on the left-hand-side quantities denotes the iteration index of the nonlinear solver.

*Multicorrector stage:* Repeat the following steps for  $i = 1, 2, \dots, i_{\max}$

(1) Evaluate the iterates at the  $\alpha$  level

$$\mathbf{C}_{n+\alpha} = \mathbf{C}_n + \alpha(\mathbf{C}_{n+1,(i-1)} - \mathbf{C}_n) \quad (65)$$

(2) Use  $\mathbf{C}_n$ ,  $\mathbf{C}_{n+\alpha}$  and  $\mathbf{V}_{n+1,(i-1)}$  to assemble the residual and the tangent matrix of the linear system

$$\begin{pmatrix} \mathbf{K}_{11,(i)} & \mathbf{K}_{12,(i)} \\ \mathbf{K}_{21,(i)} & \mathbf{K}_{22,(i)} \end{pmatrix} \begin{pmatrix} \Delta \mathbf{C}_{n+1,(i)} \\ \Delta \mathbf{V}_{n+1,(i)} \end{pmatrix} = \begin{pmatrix} \mathbf{R}_{(i)}^M \\ \mathbf{R}_{(i)}^E \end{pmatrix} \quad (66)$$

Solve this linear system using a preconditioned GMRES algorithm to a specified tolerance (see [68]).

(3) Use  $\Delta \mathbf{C}_{n+1,(i)}$  and  $\Delta \mathbf{V}_{n+1,(i)}$  to update the iterates as

$$\mathbf{C}_{n+1,(i)} = \mathbf{C}_{n+1,(i-1)} + \Delta \mathbf{C}_{n+1,(i)} \quad (67)$$

$$\mathbf{V}_{n+1,(i)} = \mathbf{V}_{n+1,(i-1)} + \Delta \mathbf{V}_{n+1,(i)} \quad (68)$$

This completes one nonlinear iteration. The nonlinear iterative algorithm should be repeated until both residuals  $\mathbf{R}^M$  and  $\mathbf{R}^E$  have been reduced to a given tolerance.

## Remarks

- (1) The concentration control variables at the initial time  $\mathbf{C}_0$  are straightforwardly obtained from the initial condition. We obtain the control variables  $\mathbf{V}_0$  by solving Eq. (21).
- (2) We use a consistent tangent matrix in our computations. Two to four nonlinear iterations are normally required to reduce the nonlinear residual to  $10^{-3}$  of its initial value in a time step.

## 3.5. Time-step adaptivity

Time-step adaptivity is of prime importance to simulate the entire dynamics of the Cahn–Hilliard equation [23,35,64] accurately and efficiently. We propose an adaptive time-stepping strategy for our provably stable scheme. The method is presented in Algorithm 1.

---

### Algorithm 1. Time step adaptive process

---

**Given:**  $\mathbf{C}_n$ ,  $\mathbf{V}_n$  and  $\Delta t_n$

- 1: Compute  $\mathbf{C}_{n+1}^{\text{BE}}$  using the Backward Euler method and  $\Delta t_n$
  - 2: Compute  $\mathbf{C}_{n+1}$  using Eqs. (26) and (27) and  $\Delta t_n$
  - 3: Calculate  $e_{n+1} = \|\mathbf{C}_{n+1}^{\text{BE}} - \mathbf{C}_{n+1}\| / \|\mathbf{C}_{n+1}\|$
  - 4: **if**  $e_{n+1} > \text{tol}$  **then**
  - 5:   Recalculate the time step  $\Delta t_n \leftarrow F(e_{n+1}, \Delta t_n)$
  - 6:   **goto** 1
  - 7: **else**
  - 8:   Update the time step  $\Delta t_{n+1} = F(e_{n+1}, \Delta t_n)$
  - 9:   **continue**
  - 10: **end if**
- 

We update the time step using the equation

$$F(e, \Delta t) = \rho \left( \frac{\text{tol}}{e} \right)^{1/2} \Delta t, \quad (69)$$



which is frequently used in adaptive time-stepping algorithms based on embedded Runge–Kutta methods [10,38,72]. Our default values for the safety coefficient  $\rho$  and the tolerance  $tol$  are those suggested in [55], that is,  $\rho = 0.9$  and  $tol = 10^{-3}$ .

**Remarks.** Note that when the accuracy criterion in Algorithm 1 (Step 4) is not satisfied, the computed solution is rejected and recalculated using a smaller time step. Typically, fewer than 10% of the time steps are rejected using the safety coefficient  $\rho = 0.9$ .

#### 4. Numerical examples

In this section we present some numerical examples that illustrate the robustness, stability, and accuracy of our numerical formulation.

For the space discretization we employ  $C^1$  quadratic Non-Uniform Rational B-Splines (NURBS) for all variables. Although, our variational formulation is well defined when  $C^0$  basis functions are employed, the  $C^1$  quadratic elements have been shown to exhibit superior approximability properties [1,19,29,46].

##### 4.1. Dimensionless form of the Cahn–Hilliard equation

To minimize the number of independent parameters in our numerical examples we will use a dimensionless form [5] of the Cahn–Hilliard equation. Introducing the arbitrary length and time scales  $L_0$  and  $T_0 = L_0^4 / (N\omega D\epsilon^2)$ , we obtain the dimensionless equation,

$$\frac{\partial \hat{c}}{\partial \hat{t}} = \hat{\nabla} \cdot (\hat{M}(\hat{c}) \hat{\nabla} (\chi \hat{\mu}(\hat{c}) - \hat{\Delta} \hat{c})), \quad (70)$$

where the “hats” indicate that the corresponding variable/operator has been nondimensionalized using the scales  $L_0$  and  $T_0$ . The rest of the notation is as follows:

$$\hat{\mu}(\hat{c}) = \hat{c} \log(\hat{c}) + (1 - \hat{c}) \log(1 - \hat{c}) + 2\theta_m \hat{c}(1 - \hat{c}) \quad (71)$$

$$\hat{M}(\hat{c}) = \hat{c}(1 - \hat{c}) \quad (72)$$

and

$$\chi = \frac{L_0^2}{2\theta_m \epsilon^2} \quad (73)$$

is a dimensionless group of the problem. As shown in [35], the thickness of the interface layers scales as  $\chi^{-1/2}$ .

The dimensionless Ginzburg–Landau free-energy is given by

$$\hat{\mathcal{E}}(\hat{c}) = \frac{\mathcal{E}(c)}{NkTL_0^3} \int_{\hat{\Omega}} \left( \hat{c} \log(\hat{c}) + (1 - \hat{c}) \log(1 - \hat{c}) + 2\theta_m \hat{c}(1 - \hat{c}) + \frac{1}{2\chi} |\hat{\nabla} \hat{c}|^2 \right) d\hat{\mathbf{x}} \quad (74)$$

We will take  $L_0 = 1$  and  $\theta_m = 3/2$  for all the numerical examples. As a consequence, the value of  $\chi$  completely characterizes the solution.

Henceforth, we will use the dimensionless form of the Cahn–Hilliard equation. Thus, let us drop the hats for the sake of notational convenience.

##### 4.2. Accuracy test

We start by verifying numerically that our method is second-order accurate in time. In order to simplify the computations, we will limit ourselves to a one-dimensional setting. The computational domain is  $\bar{\Omega} = [0, 1]$  and the spatial mesh is composed of 256 quadratic elements. We will assume that the error introduced by the space discretization is negligible. The problem is defined by  $\chi = 100$ . We set periodic boundary conditions. As initial conditions we take a randomly perturbed homogeneous concentration state. We calculated the solution at time  $t = 6.4 \cdot 10^{-3}$  (at this time the flow is fully separated) using a time step  $\Delta t = 10^{-7}$  and assumed this is the exact solution. Then, we repeated the computation with larger time steps and studied how the  $\mathcal{L}^2([0, 1])$  spatial error norm at time  $t$  evolved as a function of  $\Delta t$ . The results are presented on a doubly logarithmic scale in Fig. 1. We observe that the data defines a straight line with slope 1.99, which confirms the theoretical prediction of second-order accuracy in time.

##### 4.3. Phase separation on a periodic square: constant time step

In this example we analyze the performance of our time integration scheme for a wide range of time step sizes. We feel that this example demonstrates the robustness, accuracy and stability of our method.

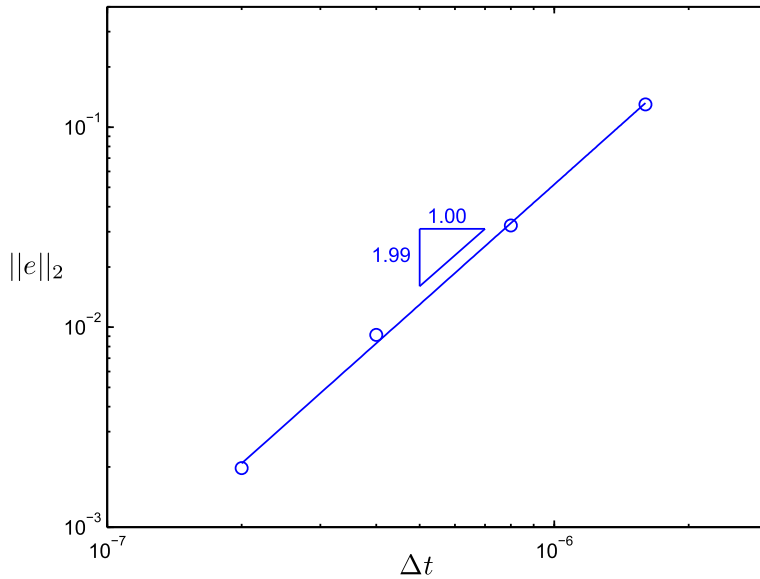


**Fig. 1.** Accuracy test.  $\mathcal{L}^2([0, 1])$  norm of the time-integration error versus time step. This plot confirms the theoretical prediction of second-order accuracy in time.

The computational domain is the square  $\bar{\Omega} = [0, 1]^2$ . The problem is defined by  $\chi = 600$ . We assume periodic boundary conditions. As initial condition, we take a randomly perturbed homogeneous concentration state  $\bar{c}$ . We set  $\bar{c} = 0.7$  in this example. The random perturbation is uniformly distributed on  $[-0.05, 0.05]$  and it is directly applied to the global vector of degrees of freedom  $C_0$ .

It is known that the Cahn–Hilliard equation is unstable under random perturbations within the spinodal region and, thus, two separate phases will develop. The dynamics of the Cahn–Hilliard equation are driven by the minimization of the Ginzburg–Landau free energy, which is composed of two terms, namely, the chemical free energy and the surface free energy. The minimization of these two components of the Ginzburg–Landau free energy occurs almost independently, and at significantly different time scales. The first part of the dynamics is phase separation. This process is driven by the minimization of the chemical free energy and takes place at very short time scales. After phase separation, the chemical free energy is essentially minimized, because the mass of the two phases is conserved during the entire process. The phenomenon that follows phase separation is known as coarsening and it is driven by the minimization of the surface free energy. When the dimensionless number  $\chi$  is very large, the minimization of the surface free energy may also be thought of as the minimization of the interface length. The process finishes when there are only two regions occupied by the two components of the mixture and they achieve the equilibrium topology. We will observe this behavior in our simulations.

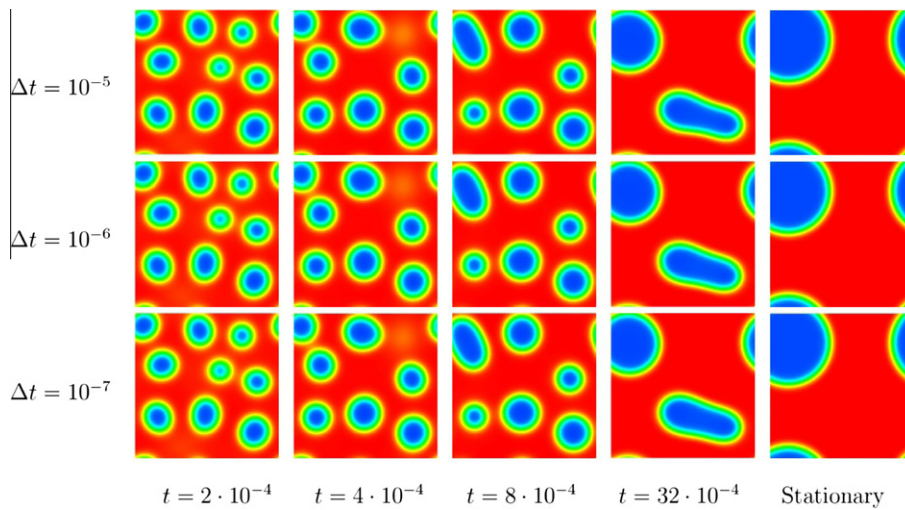
For the space discretization, we employ a uniform mesh of  $64^2$  quadratic elements in the calculations. We integrate in time using our new method and analyze its behavior for different values of the time step  $\Delta t$ . In an effort to illustrate the properties of our time integration scheme we will use constant time steps in this example, although we are aware that this is a very inefficient strategy for the Cahn–Hilliard equation.

We will compare our algorithm with the Generalized- $\alpha$  method [16,47] and Eyre's scheme. In our experience, the Generalized- $\alpha$  method is a very accurate and robust scheme, but one that is not provably stable for the Cahn–Hilliard equation. Eyre's scheme is a first-order accurate provably unconditionally stable algorithm for the Cahn–Hilliard equation.

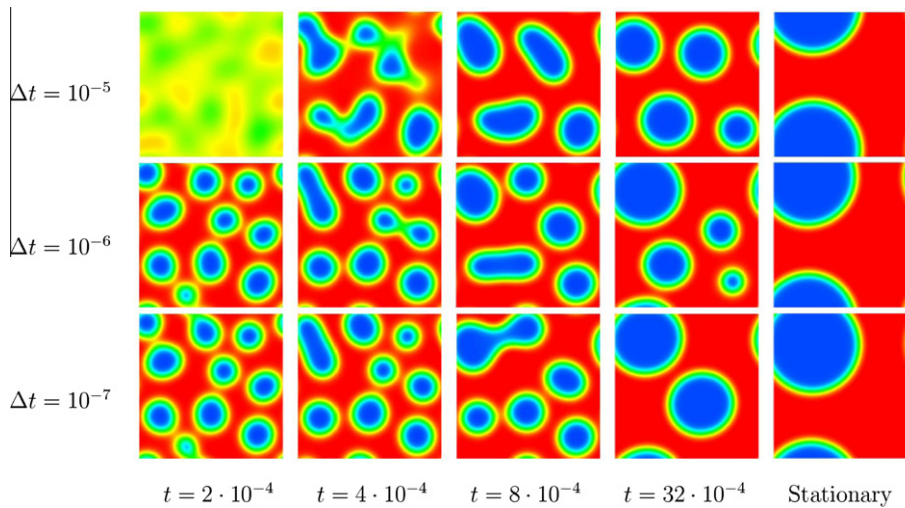
Fig. 2 shows the solution of the Cahn–Hilliard equation using the space discretization defined in (20) and (21) and the Generalized- $\alpha$  method with  $\rho_\infty = 0.5$  (see [47] for a description of the Generalized- $\alpha$  method). We have used different time steps, as shown on the left-hand side of the figure. The top row shows snapshots of the solution at different times for  $\Delta t = 10^{-5}$ , while the lower rows show the time-history of the numerical solution for  $\Delta t = 10^{-6}$  and  $\Delta t = 10^{-7}$ . There are no discernible differences between the solutions computed using different time steps. Thus, we take any of these solutions as our reference solution.

Fig. 3 shows the solution to the Cahn–Hilliard equation using the space discretization defined in (20) and (21) and Eyre's method for time integration. The implementation of the method in a mixed finite element framework follows [49]. Eyre's method is based on a splitting of the chemical free energy on a convex ( $\Psi^D$ ) and a concave ( $\Psi^P$ ) function. Although Eyre's method was originally proposed for the quartic chemical free energy, we extend it here to the logarithmic free energy to make the comparison meaningful. For the logarithmic chemical free energy there is a very natural splitting, which we adopt here. It is defined as,

$$\Psi_c = \Psi^D + \Psi^P \quad (75)$$



**Fig. 2.** Phase separation on a periodic square: constant time step. Numerical solution using the generalized- $\alpha$  method for time integration. Each row of the figure shows snapshots of the solution at the times indicated at the bottom and has been calculated using the time step indicated on the left hand side of the figure.



**Fig. 3.** Phase separation on a periodic square: constant time step. Numerical solution using Eyre's method for time integration. Each row of the figure shows snapshots of the solution at the times indicated at the bottom and has been calculated using the time step indicated on the left hand side of the figure.

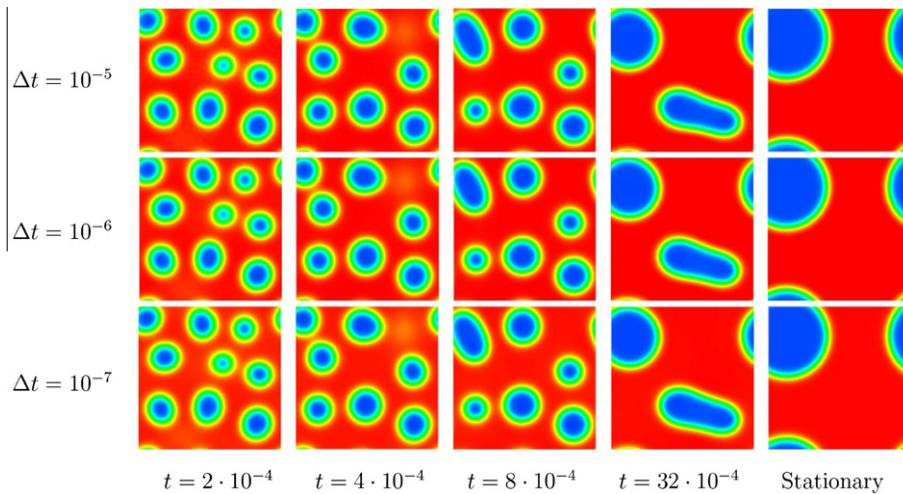
where

$$\Psi^D(c) = NkT(c \log c + (1 - c) \log(1 - c)) \quad (76)$$

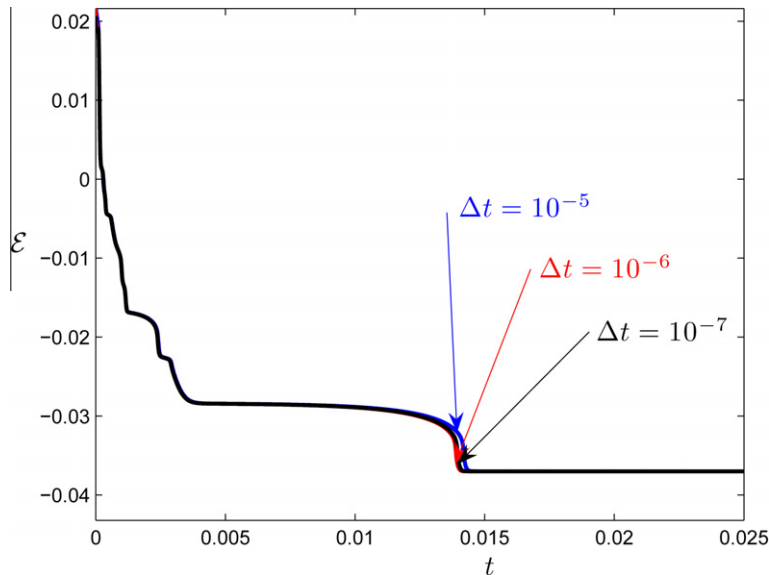
$$\Psi^P(c) = N\omega c(1 - c) \quad (77)$$

Fig. 3 presents the numerical results using Eyre's method for time integration. It shows that Eyre's method is very robust, but also significantly inaccurate. The first row shows that for  $\Delta t = 10^{-5}$  Eyre's scheme is clearly less accurate than the Generalized- $\alpha$  method. The early dynamics of the equation are completely missed by Eyre's method. The last row of the figure shows that, even for very small time steps, Eyre's method is significantly inaccurate, leading to incorrect morphologies in the phase-separation process.

In Fig. 4 we plot the transient and stationary solutions using our new method. We again use different time step sizes, as shown on the left-hand side of the figure. The top row of the figure shows the solution for  $\Delta t = 10^{-5}$ . The lower rows show snapshots of the solution for  $\Delta t = 10^{-6}$  and  $\Delta t = 10^{-7}$ , as indicated in the figure. From Figs. 2 and 4 we conclude that the accuracy of our provably stable algorithm is similar to that of the Generalized- $\alpha$  method. The solutions in Fig. 4 are indistinguishable from those obtained using the Generalized- $\alpha$  method. From Figs. 3 and 4 we conclude that our method is significantly more accurate than the most widely used provably stable method for the Cahn–Hilliard equation, namely, Eyre's algorithm.



**Fig. 4.** Phase separation on a periodic square: constant time step. Numerical solution using our provably stable method. Each row of the figure shows snapshots of the solution at the times indicated at the bottom and has been calculated using the time step indicated on the left hand side of the figure.



**Fig. 5.** Phase separation on a periodic square: constant time step. Evolution of the Ginzburg–Landau free energy calculated using our provably stable algorithm. We represent three curves, each corresponding to the time step labeled. We observe that the free energy does not increase with time irrespectively of the time step.

Finally, Fig. 5 shows the evolution of the Ginzburg–Landau free energy using our time integration algorithm. We plot three energy curves that correspond to different time steps, as indicated in the figure. We observe that the free energy does not increase with time, even for very large time steps. This supports our theoretical results.

#### Remark

- (1) We have also performed this calculation using standard second-order accurate time integration schemes, such as the trapezoidal rule and the midpoint rule. These methods led to unstable results for  $\Delta t = 10^{-5}$  and produced similar results to those of our method for  $\Delta t = 10^{-6}$  and  $\Delta t = 10^{-7}$ . This fact shows that our algorithm permits using larger time steps than those necessary for standard second-order accurate time integration schemes.
- (2) We have corroborated numerically that our method verifies mass conservation. The maximum relative error in mass conservation over the entire dynamical process is of the order of  $10^{-7}$ , which may be attributed to the tolerance of the nonlinear solver or numerical integration.

#### 4.4. Phase separation on a periodic square: adaptive time step

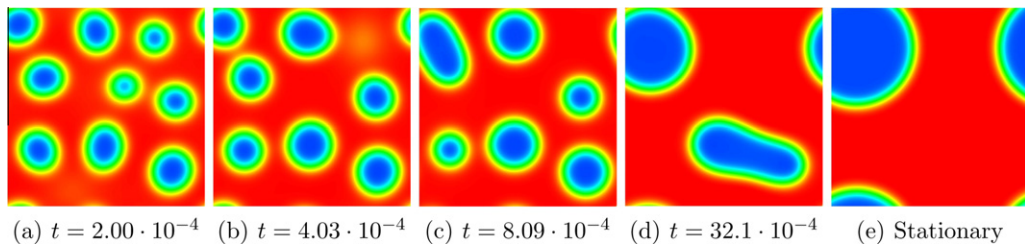
In this section we recompute the previous example using our adaptive time-stepping algorithm. Our goal is to show that the proposed time integration scheme may be easily combined with an adaptive technique, rendering an accurate, efficient and provably stable algorithm.

Fig. 6 shows snapshots of the solution at different times and the stationary configuration. The images are all indistinguishable from those calculated with a constant time step  $\Delta t = 10^{-7}$  (see Fig. 4). We note that there are significantly fewer time steps taken in the adaptive case.

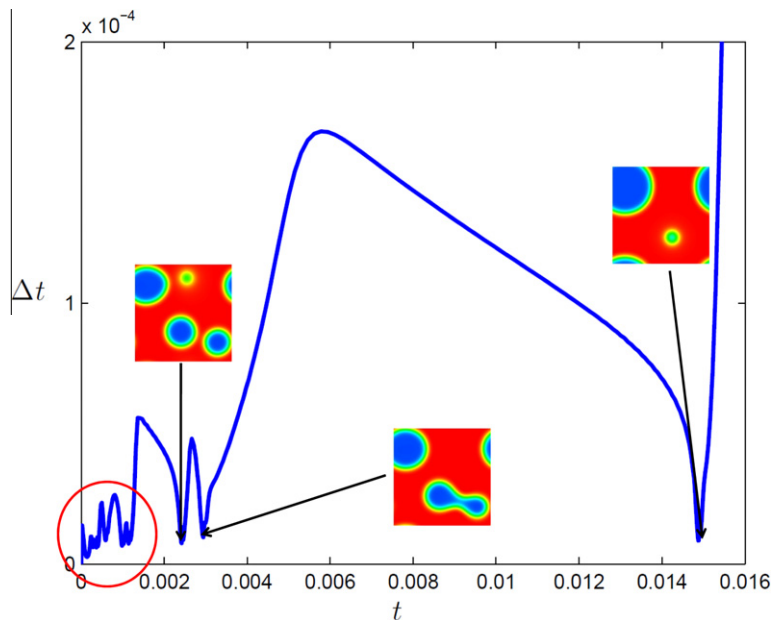
The evolution of the time step may be observed in Fig. 7. As we had anticipated, we observe two main processes that take place at very different time scales, namely, phase separation and coarsening. Phase separation takes place at the beginning of the simulation and corresponds to the initial part of the dynamics marked with a circle in Fig. 7. During the coarsening process that follows phase separation, bubbles merge with each other to reduce the surface energy.

Fig. 7 shows a complex pattern in the evolution of the time step. This pattern is actually reflecting the physics of the problem. Every local minimum in the time step in Fig. 7 corresponds to a significant dynamical event in the evolution of the mixture. We observe that the three main local minima in Fig. 7 (these are marked with arrows in the figure with accompanying snapshots of the solution) correspond to either the disappearance of a bubble or to the coalescence of two bubbles. These are the two main mechanisms by which coarsening takes place.

Let us now look at the small area marked with a circle in Fig. 7. We have zoomed in this area and plotted it in Fig. 8. We observe again that every local minimum of the time step corresponds to a significant dynamical event (see the snapshots of



**Fig. 6.** Phase separation on a periodic square: adaptive time step. Numerical solution using our provably stable method. The solution is indistinguishable from those calculated using a constant time step  $\Delta t = 10^{-7}$ .



**Fig. 7.** Phase separation on a periodic square: adaptive time step. Evolution of the time step using our adaptive provably stable algorithm. We depict snapshots of the solution appended to the time-step curve. These show that local minima in the time step correspond to significant dynamical events in the evolution of the mixture.



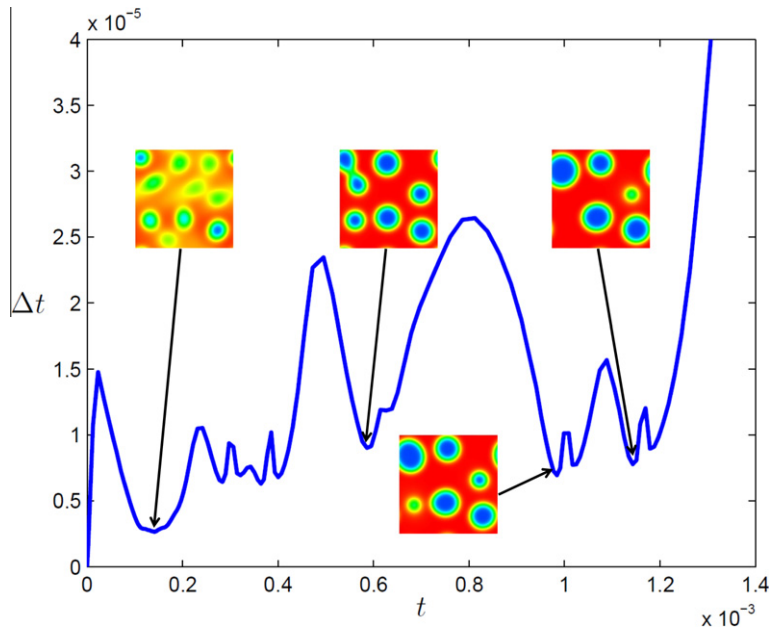


**Fig. 8.** Phase separation on a periodic square: adaptive time step. Detail of the evolution of the time step using the adaptive provably stable algorithm. Snapshots of the solution accompany the time-step curve. These show that local minima in the time step correspond to significant dynamical events in the evolution of the mixture.

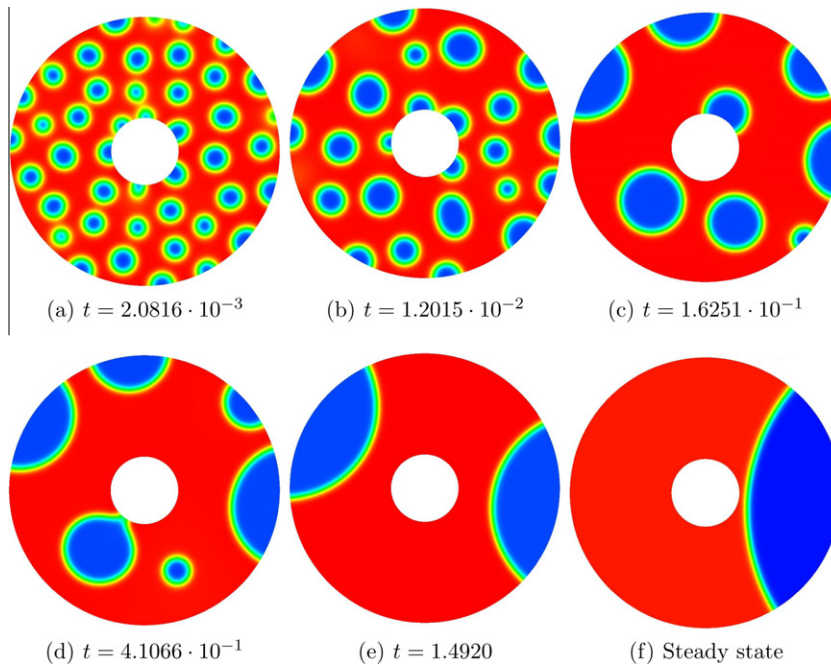


**Fig. 9.** Phase separation on an annular surface: solution at different times and steady-state configuration using our new provably stable algorithm.

the solution that accompany the time-step curve). In particular, the first local minimum corresponds to phase separation. The subsequent local minima correspond to either the disappearance of a bubble or the coalescence of two bubbles.

#### Remarks

- (1) In this example the ratio  $\Delta t/\delta$  varies from approximately  $0.142 \cdot 10^{-5}$  to  $0.537$ , demonstrating the good performance of our method for a wide range of values of  $\Delta t/\delta$ .

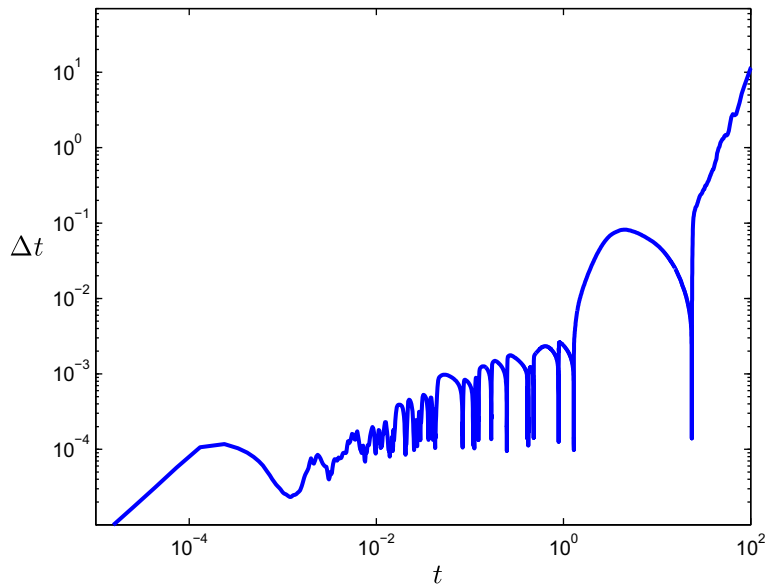


**Fig. 10.** Phase separation on an annular surface. Evolution of time step on a doubly logarithmic scale. We use our adaptive provably stable algorithm.

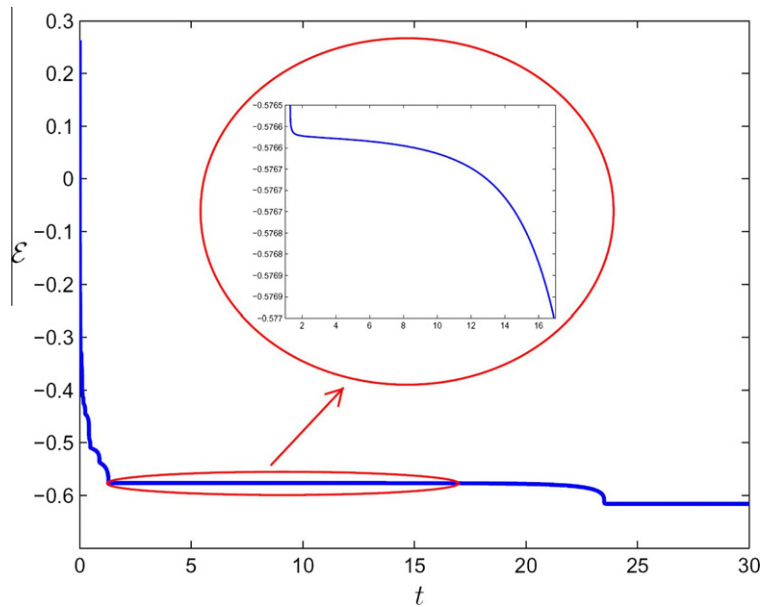


**Fig. 11.** Phase separation on an annular surface. Evolution of the Ginzburg–Landau free energy using our new adaptive provably stable algorithm. We have zoomed in the part of the evolution between  $t = 1$  and  $t = 16$  because it appears almost flat at the scale of the plot. The figure clearly shows that the free energy does not increase at any time.

- (2) The evolution of the time step depicted in Fig. 7 is fairly complex. However, it corresponds to a simple example of the Cahn–Hilliard equation. The dynamics of the Cahn–Hilliard equation become much more complex as  $\chi$  increases because the smoothness of the interface layer is reduced and the range of relevant length and time scales of the equation is wider (see for example [35]) and, thus, time-step adaptivity becomes even more important.

#### 4.5. Phase separation on an annular surface

In this example we solve the Cahn–Hilliard equation on an annular surface. The objective of this example is to show that our numerical formulation may be applied to non-trivial geometries while maintaining its accuracy, stability and robustness.

The interior radius of the annular surface is  $r_i = 0.5$ , while the exterior is  $r_e = 2$ . We employ a uniform mesh composed of 256 elements in the circumferential direction and 64 in the radial direction. We use quadratic NURBS, which permit exact geometrical modeling of this problem. On the boundary we weakly enforce natural boundary conditions by way of (18) and (19).

The initial condition is a randomly perturbed homogeneous concentration state  $\bar{c}$ . We take  $\bar{c} = 0.7$  and a random perturbation uniformly distributed on  $[-0.05, 0.05]$ . In this example we take the value  $\chi = 200$ .

We use the discrete formulation (26) and (27) and adaptive time stepping. Fig. 9 shows several snapshots of the time-history of the numerical solution. The physical process is the same as in the previous example and we observe again phase separation followed by coarsening.

In Fig. 10 we plot the evolution of the time step on a doubly logarithmic scale. We observe a richer behavior than in the previous example and larger variations of the time step. In this example the ratio  $\Delta t/\delta$  varies from approximately  $1.693 \cdot 10^{-7}$  to  $2.941 \cdot 10^1$ , showing the good performance of our algorithm for a wide range of values of  $\Delta t/\delta$ .

Fig. 11 shows the evolution of the Ginzburg–Landau free energy. We have zoomed in on the part of the evolution between  $t = 1$  and  $t = 16$  because it looked almost flat at the scale of the plot. The figure clearly shows that the free energy does not increase at any time.

## 5. Conclusions

We have introduced provably unconditionally stable, second-order time accurate, mixed variational methods for phase-field models. Our numerical formulation is based on a mixed finite element formulation for the space discretization and a new second-order accurate time integration scheme. We prove that our formulation inherits the main characteristics of conserved phase dynamics, namely, mass conservation and nonlinear stability with respect to the free energy. We also propose an adaptive time-stepping algorithm that may be easily combined with our method. We present numerical examples that illustrate the robustness, accuracy and stability of our formulation.

## Acknowledgements

H. Gomez was partially supported by the J. Tinsley Oden Faculty Fellowship Research Program at the Institute for Computational Engineering and Sciences. H. Gomez gratefully acknowledges the funding provided by *Xunta de Galicia* (grants #09REM005118PR and #09MDS00718PR), *Ministerio de Ciencia e Innovación* (grants #DPI2009-14546-C02-01 and #DPI2010-16496) cofinanced with FEDER funds, and *Universidad de A Coruña*. T.J.R. Hughes was partially supported by the Office of Naval Research under Contract Number N00014-08-1-0992.

## Appendix A

In this appendix we derive the following quadrature formula:

$$\int_a^b f(x) dx = \frac{b-a}{2} (f(a) + f(b)) - \frac{(b-a)^3}{12} f''(a) - \frac{(b-a)^4}{24} f'''(\xi); \quad \xi \in (a, b) \quad (78)$$

where  $f : [a, b] \mapsto \mathbb{R}$  is a sufficiently smooth function.

Let  $P_2$  be the quadratic polynomial that satisfies

$$P_2(a) = f(a); \quad P_2(b) = f(b); \quad P_2''(a) = f''(a) \quad (79)$$

We define the function  $R_2$  as,

$$R_2(x) = f(x) - P_2(x) \quad (80)$$

From the definition of  $R_2$  and  $P_2$  it follows that

$$R_2(a) = R_2(b) = 0 \quad (81)$$

Let us rewrite  $R_2$  as

$$R_2(x) = w_2(x) S_2(x) \quad (82)$$

where

$$w_2(x) = (x-a)(x-b)(x+b-2a) \quad (83)$$

and  $S_2$  is an unknown function such that (82) is verified. For further reference, we note that  $w_2$  verifies the conditions  $w_2(a) = w_2(b) = w_2''(a) = 0$ .

Let us define the function

$$F(z) = f(z) - P_2(z) - w_2(z) S_2(x) \quad (84)$$



where  $x$  is a fixed parameter. This function clearly satisfies the conditions  $F(a) = F(b) = F(x) = 0$ . Applying Rolle's theorem twice we conclude there exists at least one point in the open interval  $(a, b)$  at which  $F'$  vanishes. In addition, we know that  $F''(a) = 0$ , which allows us to apply Rolle's theorem again to conclude that there exists  $\theta \in (a, b)$  such that  $F'''(\theta) = 0$ . Taking derivatives in Eq. (84) we can obtain an explicit expression for  $F'''$ , namely

$$F'''(z) = f'''(z) - \underbrace{w_2'''(z)}_{=6} S_2(x) \quad (85)$$

Evaluating this expression at  $z = \theta$ , it follows that

$$S_2(x) = \frac{f'''(\theta)}{6} \quad (86)$$

Taking all of this into account, we may integrate (80) to conclude

$$\int_a^b f(x) dx = \int_a^b P_2(x) dx + \int_a^b w_2(x) \frac{f'''(\theta(x))}{6} dx \quad (87)$$

Since  $w_2$  does not change sign on the open interval  $(a, b)$ , we can apply the mean value theorem to the last integral in (87) to obtain

$$\int_a^b w_2(x) \frac{f'''(\theta(x))}{6} dx = \frac{f'''(\xi)}{6} \int_a^b w_2(x) dx; \quad \xi \in (a, b) \quad (88)$$

This analysis leads to the quadrature formula

$$\int_a^b f(x) dx = \frac{b-a}{2} (f(a) + f(b)) - \frac{(b-a)^3}{12} f''(a) - \frac{(b-a)^4}{24} f'''(\xi); \quad \xi \in (a, b) \quad (89)$$

## References

- [1] I. Akkerman, Y. Bazilevs, V.M. Calo, T.J.R. Hughes, S. Hulshoff, The role of continuity in residual-based variational multiscale modeling of turbulence, *Computational Mechanics* 41 (2007) 371–378.
- [2] D.M. Anderson, G.B. McFadden, A.A. Wheeler, Diffuse-interface methods in fluid mechanics, *Annual Review of Fluid Mechanics* 30 (1998) 139–165.
- [3] F. Armero, C. Zambrana-Rojas, Volume-preserving energy-momentum schemes for isochoric multiplicative plasticity, *Computer Methods in Applied Mechanics and Engineering* 196 (2007) 4130–4159.
- [4] F. Auricchio, L. Beirão da Veiga, T.J.R. Hughes, A. Reali, G. Sangalli, Isogeometric collocation methods, *Mathematical Models and Methods in Applied Sciences* 2 (2010) 2075–2107.
- [5] G.I. Barenblatt, *Scaling, Self-similarity, and Intermediate Asymptotics*, Cambridge University Press, 1996.
- [6] Y. Bazilevs, V.M. Calo, J.A. Cottrell, J.A. Evans, T.J.R. Hughes, S. Lipton, M.A. Scott, T.W. Sederberg, Isogeometric Analysis using T-splines, *Computer Methods in Applied Mechanics and Engineering* 199 (2010) 229–263.
- [7] Y. Bazilevs, V.M. Calo, J.A. Cottrell, T.J.R. Hughes, A. Reali, G. Scovazzi, Variational multiscale residual-based turbulence modeling for large eddy simulation of incompressible flows, *Computer Methods in Applied Mechanics and Engineering* 197 (2007) 173–201.
- [8] Y. Bazilevs, T.J.R. Hughes, NURBS-based isogeometric analysis for the computation of flows about rotating components, *Computational Mechanics* 43 (2008) 143–150.
- [9] J. Becker, G. Grün, R. Seemann, H. Mantz, K. Jacobs, K.R. Mecke, R. Blossey, Complex dewetting scenarios captured by thin-film models, *Nature Materials* 2 (2003) 59–63.
- [10] G. Benderskaya, M. Clemens, H. De Gersem, T. Weiland, Embedded Runge–Kutta methods for field-circuit coupled problems with switching elements, *IEEE Transactions on Magnetics* 41 (2005) 1612–1615.
- [11] A. Buffa, G. Sangalli, R. Vázquez, Isogeometric analysis in electromagnetics: B-splines approximation, *Computer Methods in Applied Mechanics and Engineering* 199 (2010) 1143–1152.
- [12] J.W. Cahn, J.E. Hilliard, Free energy of a non-uniform system. I. Interfacial free energy, *The Journal of Chemical Physics* 28 (1958) 258–267.
- [13] J.W. Cahn, J.E. Hilliard, Free energy of a non-uniform system. III. Nucleation in a two-component incompressible fluid, *The Journal of Chemical Physics* 31 (1959) 688–699.
- [14] L.Q. Chen, Phase-field models for microstructural evolution, *Annual Review Materials Research* 32 (2002) 113–140.
- [15] R. Choksi, M.A. Peletier, J.F. Williams, On the phase diagram for microphase separation of diblock copolymers: an approach via a nonlocal Cahn–Hilliard functional, *SIAM Journal of Applied Mathematics* 69 (2009) 1712–1738.
- [16] J. Chung, G.M. Hulbert, A time integration algorithm for structural dynamics with improved numerical dissipation: the generalized- $\alpha$  method, *Journal of Applied Mechanics* 60 (1993) 371–375.
- [17] M.I.M. Copetti, C.M. Elliott, Numerical analysis of the Cahn–Hilliard equation with a logarithmic free energy, *Numerische Mathematik* 63 (1992) 39–65.
- [18] J.A. Cottrell, T.J.R. Hughes, Y. Bazilevs, *Isogeometric Analysis: Toward integration of CAD and FEA*, Wiley, 2009.
- [19] J.A. Cottrell, T.J.R. Hughes, A. Reali, Studies of refinement and continuity in isogeometric structural analysis, *Computer Methods in Applied Mechanics and Engineering* 196 (2007) 4160–4183.
- [20] V. Cristini, X. Li, J.S. Lowengrub, S.M. Wise, Nonlinear simulations of solid tumor growth using a mixture model: invasion and branching, *Journal of Mathematical Biology* 58 (2009) 723–763.
- [21] L. Cueto-Felgueroso, R. Juanes, Nonlocal interface dynamics and pattern formation in gravity-driven unsaturated flow through porous media, *Physical Review Letters* 101 (2008) 244504.
- [22] L. Cueto-Felgueroso, R. Juanes, A phase-field model of unsaturated flow, *Water Resources Research* 45 (2009) W10409.
- [23] L. Cueto-Felgueroso, J. Peraire, A time-adaptive finite volume method for the Cahn–Hilliard and Kuramoto–Sivashinsky equations, *Journal of Computational Physics* 227 (2008) 9985–10017.
- [24] Q. Du, R.A. Nicolaides, Numerical analysis of a continuum model of phase transition, *SIAM Journal of Numerical Analysis* 28 (1991) 1310–1322.
- [25] T. Elguedj, Y. Bazilevs, V.M. Calo, T.J.R. Hughes,  $\bar{B}$  and  $\bar{F}$  projection methods for nearly incompressible linear and non-linear elasticity and plasticity using higher-order NURBS elements, *Computer Methods in Applied Mechanics and Engineering* 197 (2008) 2732–2762.
- [26] C.M. Elliott, H. Garcke, On the Cahn–Hilliard equation with degenerate mobility, *SIAM Journal of Mathematical Analysis* 27 (1996) 404–423.
- [27] H. Emmerich, *The Diffuse Interface Approach in Materials Science*, Springer, 2003.

- [28] D.J. Eyre, An unconditionally stable one-step scheme for gradient systems, unpublished. <[www.math.utah.edu/~eyre/research/methods/stable.ps](http://www.math.utah.edu/~eyre/research/methods/stable.ps)>
- [29] J.A. Evans, Y. Bazilevs, I. Babuška, T.J.R. Hughes, n-widths, sup infs, and optimality ratios for the k-version of the isogeometric finite element method, *Computer Methods in Applied Mechanics and Engineering* 198 (2009) 1726–1741.
- [30] X. Feng, H. Wu, A posteriori error estimates for finite element approximations of the Cahn–Hilliard equation and the Hele–Shaw flow, *Journal of Computational Mathematics* 26 (2008) 767–796.
- [31] I. Fonseca, M. Morini, Surfactants in foam stability: a phase field model, *Archive for Rational Mechanics* 183 (2007) 411–456.
- [32] H.B. Friboes, J.S. Lowengrub, S. Wise, X. Zheng, P. Macklin, E.L. Bearer, V. Cristini, Computer simulation of glioma growth and morphology, *NeuroImage* 37 (2007) 59–70.
- [33] E. Fried, M.E. Gurtin, Dynamic solid–solid transitions with phase characterized by an order parameter, *Phys. D* 72 (1994) 287–308.
- [34] D. Furihata, A stable and conservative finite difference scheme for the Cahn–Hilliard equation, *Numerische Mathematik* 87 (2001) 675–699.
- [35] H. Gomez, V.M. Calo, Y. Bazilevs, T.J.R. Hughes, Isogeometric analysis of the Cahn–Hilliard phase-field model, *Computer Methods in Applied Mechanics and Engineering* 197 (2008) 4333–4352.
- [36] H. Gomez, T.J.R. Hughes, X. Nogueira, V.M. Calo, Isogeometric analysis of the isothermal Navier–Stokes–Korteweg equations, *Computer Methods in Applied Mechanics and Engineering* 199 (2010) 1828–1840.
- [37] M.E. Gurtin, Generalized Ginzburg–Landau and Cahn–Hilliard equations based on a microforce balance, *Physica D* 92 (1996) 178–192.
- [38] K. Gustafsson, Control-theoretic techniques for stepsize selection in implicit Runge–Kutta methods, *ACM Transactions on Mathematical Software* 20 (1994) 496–517.
- [39] A. Harten, On the symmetric form of systems of conservation laws with entropy, *Journal of Computational Physics* 49 (1983) 151–164.
- [40] L. He, Y. Liu, A class of stable spectral methods for the Cahn–Hilliard equation, *Journal of Computational Physics* 228 (2009) 5101–5110.
- [41] Z. Hu, S.M. Wise, C. Wang, J.S. Lowengrub, Stable and efficient finite-difference nonlinear multigrid schemes for the phase field crystal equation, *Journal of Computational Physics* 228 (2009) 5323–5339.
- [42] J.E. Huber, N.A. Fleck, C.M. Landis, R.M. McMeeking, A constitutive model for ferroelectric polycrystals, *Journal of the Mechanics and Physics of Solids* 47 (2009) 1663–1697.
- [43] T.J.R. Hughes, *The Finite Element Method: Linear Static and Dynamic Finite Element Analysis*, Dover Publications, Mineola, NY, 2000.
- [44] T.J.R. Hughes, J.A. Cottrell, Y. Bazilevs, Isogeometric analysis: CAD, finite elements, NURBS, exact geometry and mesh refinement, *Computer Methods in Applied Mechanics and Engineering* 194 (2005) 4135–4195.
- [45] T.J.R. Hughes, L.P. Franca, M. Mallet, A new finite element formulation for computational fluid dynamics: I. Symmetric forms of the compressible Euler and Navier–Stokes equations and the second law of thermodynamics, *Computer Methods in Applied Mechanics and Engineering* 54 (1986) 223–234.
- [46] T.J. R Hughes, A. Reali, G. Sangalli, Duality and unified analysis of discrete approximations in structural dynamics and wave propagation: comparison of p-method finite elements with k-method NURBS, *Computer Methods in Applied Mechanics and Engineering* 197 (2008) 4104–4124.
- [47] K.E. Jansen, C.H. Whiting, G.M. Hulbert, A generalized- $\alpha$  method for integrating the filtered Navier–Stokes equations with a stabilized finite element method, *Computer Methods in Applied Mechanics and Engineering* 190 (1999) 305–319.
- [48] J.-H. Jeong, N. Goldenfeld, J.A. Dantzig, Phase field model for three-dimensional dendritic growth with fluid flow, *Physical Review E* 64 (2001) 1–14.
- [49] D. Kay, R. Welford, A multigrid finite element solver for the Cahn–Hilliard equation, *Journal of Computational Physics* 212 (2006) 288–304.
- [50] J. Kim, A numerical method for the Cahn–Hilliard equation with a variable mobility, *Communications in Nonlinear Science and Numerical Simulation* 12 (2007) 1560–1571.
- [51] Y.-T. Kim, N. Provatas, N. Goldenfeld, J.A. Dantzig, universal dynamics of phase field models for dendritic growth, *Physical Review E* 59 (1999) 2546–2549.
- [52] R. Kobayashi, A numerical approach to three-dimensional dendritic solidification, *Experimental Mathematics* 3 (1994) 59–81.
- [53] L.D. Landau, V.I. Ginzburg, On the theory of superconductivity, in: *Collected papers of L.D. Landau*, D. ter Haar, ed., Pergamon Oxford (1965) 626–633.
- [54] C.M. Landis, Fully coupled multi-axial, symmetric constitutive laws for polycrystalline ferroelectric ceramics, *Journal of the Mechanics and Physics of Solids* 50 (2002) 127–152.
- [55] J. Lang, Two-dimensional fully adaptive solutions of reaction–diffusion equations, *Applied Numerical Mathematics* 18 (1995) 223–240.
- [56] S. Lipton, J.A. Evans, Y. Bazilevs, T. Elguedj, T.J.R. Hughes, Robustness of isogeometric structural discretizations under severe mesh distortion, *Computer Methods in Applied Mechanics and Engineering* 199 (2010) 357–373.
- [57] D.R. Mahapatra, R.V.N. Melnik, Finite element analysis of phase transformation dynamics in shape memory alloys with a consistent Landau–Ginzburg free energy model, *Mechanics of Advanced Materials and Structures* 13 (2006) 443–455.
- [58] D.R. Mahapatra, R.V.N. Melnik, Finite element approach to modelling evolution of 3D shape memory materials, *Mathematics and Computers in Simulation* 76 (2007) 141–148.
- [59] E.V.L. de Mello, O. Teixeira da Silveira Filho, Numerical study of the Cahn–Hilliard equation in one, two and three dimensions, *Physica A* 347 (2005) 429–443.
- [60] X.N. Meng, T.A. Laursen, Energy consistent algorithms for dynamic finite deformation plasticity, *Computer Methods in Applied Mechanics and Engineering* 191 (2002) 1639–1675.
- [61] J.T. Oden, A. Hawkins, S. Prudhomme, General diffuse-interface theories and an approach to predictive tumor growth modeling, *Mathematical Models and Methods in Applied Sciences* 20 (2010) 477–517.
- [62] O. Penrose, P.C. Fife, Thermodynamically consistent models of phase field type for the kinetics of phase transition, *Physica D* 43 (1990) 44–62.
- [63] L. Piegl, W. Tiller, *The NURBS Book*, Monographs in Visual Communication, Springer-Verlag, 1997.
- [64] A. Rajagopal, P. Fischer, E. Kuhl, P. Steinmann, Natural element analysis of the Cahn–Hilliard phase-field model, *Computational Mechanics* 46 (2010) 471–493.
- [65] D.F. Rogers, *An Introduction to NURBS With Historical Perspective*, Academic Press, 2001.
- [66] I. Romero, Algorithms for coupled problems that preserve symmetries and the laws of thermodynamics: Part I: Monolithic integrators and their application to finite strain thermoelasticity, *Computer Methods in Applied Mechanics and Engineering* 199 (2010) 1841–1858.
- [67] I. Romero, Algorithms for coupled problems that preserve symmetries and the laws of thermodynamics: Part II: Fractional step methods, *Computer Methods in Applied Mechanics and Engineering* 199 (2010) 2235–2248.
- [68] Y. Saad, M.H. Schultz, GMRES: a generalized minimal residual algorithm for solving nonsymmetric linear systems, *SIAM Journal of Scientific and Statistical Computing* 7 (1986) 856–869.
- [69] F. Shakib, T.J.R. Hughes, Z. Johan, A new finite element formulation for computational fluid-dynamics. 10. The compressible Euler and Navier–Stokes equations, *Computer Methods in Applied Mechanics and Engineering* 89 (1991) 141–219.
- [70] E. Tadmor, Skew-self adjoint form for systems of conservation laws, *Journal of Mathematical Analysis and Applications* 103 (1984) 428–442.
- [71] S. Tremaine, On the origin of irregular structure in Saturn’s rings, *Astronomical Journal* 125 (2003) 894–901.
- [72] P.J. van der Houwen, B.P. Sommeijer, W. Couzy, Embedded diagonally implicit Runge–Kutta algorithms on parallel computers, *Mathematics of Computation* 58 (1992) 135–159.
- [73] B.P. Vollmayr-Lee, A.D. Rutenberg, Fast and accurate coarsening simulation with an unconditionally stable time step, *Physical Review E* 68 (2003) 066703.
- [74] G.N. Wells, E. Kuhl, K. Garikipati, A discontinuous Galerkin method for the Cahn–Hilliard equation, *Journal of Computational Physics* 218 (2006) 860–877.
- [75] C. Xu, T. Tang, Stability analysis of large time-stepping methods for epitaxial growth models, *SIAM Journal of Numerical Analysis* 44 (2006) 1759–1779.
- [76] J.D. van der Waals, The thermodynamic theory of capillarity under the hypothesis of a continuous variation of density, *Journal of Statistical Physics* 20 (1979) 197–244.